

Physical Properties of OSIRIS-REx Target Asteroid (101955) 1999 RQ₃₆

derived from *Herschel*^{*}, *ESO-VISIR*^{**} and *Spitzer* observations

T. G. Müller¹, L. O’Rourke², A. M. Barucci³, A. Pál⁴, C. Kiss⁴, P. Zeidler⁵, B. Altieri², B. M. González-García⁶, and
M. Küppers²

¹ Max-Planck-Institut für extraterrestrische Physik (MPE), Giessenbachstrasse, 85748 Garching, Germany; e-mail: tmueller@mpe.mpg.de

² European Space Astronomy Centre (ESAC), European Space Agency, Apartado de Correos 78, 28691 Villanueva de la Cañada, Madrid, Spain

³ Observatoire de Paris, Laboratoire d’Etudes Spatiales et d’Instrumentation en Astrophysique (LESIA), 5 Place Jules Janssen, 92195 Meudon Cedex, France

⁴ Konkoly Observatory, Research Center for Astronomy and Earth Sciences, Hungarian Academy of Sciences; Konkoly Thege 15-17, H-1121 Budapest, Hungary

⁵ Ludwig-Maximilians-Universität München, Fakultät für Physik, Schellingstraße 4, D-80799 München, Germany

⁶ INSA at European Space Astronomy Centre (ESAC), European Space Agency, Apartado de Correos 78, 28691 Villanueva de la Cañada, Madrid, Spain

Received ; accepted

ABSTRACT

In September 2011, the *Herschel* Space Observatory performed an observation campaign with the PACS photometer observing the asteroid (101955) 1999 RQ₃₆ in the far infrared. The *Herschel* observations were analysed, together with *ESO VLT-VISIR* and *Spitzer-IRS* data, by means of a thermophysical model in order to derive the physical properties of 1999 RQ₃₆. We find the asteroid has an effective diameter in the range 480 to 511 m, a slightly elongated shape with a semi-major axis ratio of $a/b=1.04$, a geometric albedo of $0.045^{+0.015}_{-0.012}$, and a retrograde rotation with a spin vector between -70 and -90° ecliptic latitude. The thermal emission at wavelengths below $12\mu\text{m}$ -originating in the hot sub-solar region- shows that there may be large variations in roughness on the surface along the equatorial zone of 1999 RQ₃₆, but further measurements are required for final proof. We determine that the asteroid has a disk-averaged thermal inertia of $\Gamma=650\text{Jm}^{-2}\text{s}^{-0.5}\text{K}^{-1}$ with a $3\text{-}\sigma$ confidence range of 350 to $950\text{Jm}^{-2}\text{s}^{-0.5}\text{K}^{-1}$, equivalent to what is observed for 25143 Itokawa and suggestive that 1999 RQ₃₆ has a similar surface texture and may also be a rubble-pile in nature. The low albedo indicates that 1999 RQ₃₆ very likely contains primitive volatile-rich material, consistent with its spectral type, and that it is an ideal target for the OSIRIS-REx sample return mission.

Key words. Minor planets, asteroids: individual – Radiation mechanisms: Thermal – Techniques: photometric – Infrared: planetary systems

1. Introduction

On May 25, 2011, NASA announced the selection of OSIRIS-REx as the third selected mission of its New Frontiers Program. The OSIRIS-REx mission will be launched in September 2016, fly by the Earth for a gravity assist in September 2017, and encounter the near-Earth asteroid (NEA) (101955) 1999 RQ₃₆ (Lauretta et al. 2010) in November 2019. Proximity operations at the asteroid last through March 2021, when it will acquire up to 2 kg sample of its surface material. The sample return capsule will return to the Earth’s surface in September 2023.

Based on its visible spectrum, 1999 RQ₃₆ is classified as a B-type and CM chondrite meteorites are considered to be the corresponding spectral analog (Clark et al. 2011). B-class asteroids are found mostly in the middle and outer regions of the main

belt and are believed to be primitive and volatile-rich. However, the Polana family in the inner belt contains B-types, and dynamical studies have shown that 1999 RQ₃₆ might be a liberated member of this family, considered as an important inner-belt source of low-albedo NEAs (Campins et al. 2010; Cellino et al. 2001). Additionally, since its orbit makes it especially accessible to spacecraft and it has been identified as a potentially hazardous asteroid (Milani et al. 2009), it was considered an ideal choice for NASA’s OSIRIS-REx sample return mission (Lauretta et al. 2012).

Radar images, taken during its previous two closest approaches in 1999 and in 2005 (and the next occurred in September 2011 when our observations were performed) found 1999 RQ₃₆ to be an irregular spheroid about 580 m in diameter (Nolan et al. 2007). The nearly spheroidal shape suggests that it might be a strengthless rubble pile, formed by mechanisms similar to near-Earth binary systems (Walsh et al. 2008). The latest analysis, where all available radar data was combined with visible lightcurves (Nolan et al. 2012), derived a mean diameter of 493 ± 20 m (mean equatorial diameter of 545 ± 15 m) and a

* *Herschel* is an ESA space observatory with science instruments provided by European-led Principal Investigator consortia and with important participation from NASA.

** Analysis is also based on observations collected at the European Southern Observatory, Chile; ESO, No. 287.C-5045(A)

“spinning top” shape similar to 1999 KW₄ (Ostro et al. 2006), but with a less well-defined equatorial ridge.

The object’s rotation period is 4.297812 ± 0.000001 hours (Nolan et al. 2012), which was derived from combined radar and lightcurve measurements. This period is very similar to the 4.288 h found by Nolan et al. (2007) from radar measurements alone and to the 4.2968 ± 0.0017 h based on the analysis of lightcurves (Hergenrother et al. 2012) and about twice the value given in Krugly et al. (2002) derived from incomplete R-band lightcurve observations during the 1999 opposition. The rotation period suggests that it has not been greatly spun up by tidal or radiation forces. However, the radar-derived pole orientation ($\beta_{pole} = -90^\circ \pm 15^\circ$) is the equilibrium state for the YORP effect (Vokrouhlický et al. 2003). The negative pole orientation indicates a retrograde rotation.

Emery et al. (2010) find a size of 610 m and estimate its thermal inertia to be around $600 \text{ J m}^{-2} \text{ s}^{-0.5} \text{ K}^{-1}$, assuming a moderate surface roughness (*r.m.s.*-slopes $\sim 20^\circ$). Their results are based on Spitzer-IRS spectra and a dual-band thermal lightcurve, taken on May 3/4, 2007 at a phase angle of about 63° .

In this paper, we first present our PACS and ESO-VISIR Director Discretionary awarded Time (DDT) observations taken of 1999 RQ₃₆ and their data reduction. We follow this with the description of the Spitzer-IRS measurements and the corresponding data reduction. We analyse the derived flux densities by means of our thermal model. We proceed to present our radiometrically derived properties (Section 3). In Section 4 we discuss the object’s size, shape, and albedo in a wider context and study the influences of surface roughness and thermal inertia in detail. We finally conclude the paper with a summary of all derived properties and with the implications of our results for the preparations for the OSIRIS-REx mission.

2. Observations of 1999 RQ₃₆

2.1. Herschel-PACS observations and data processing

The European Space Agency’s (ESA) Herschel Space Observatory (Pilbratt et al. 2010), launched in 2009, performs observations from the 2nd Lagrangian point (L2) at $1.5 \cdot 10^6$ km from Earth. It has three science instruments on board covering the far-infrared part of the spectrum, of which the PACS Photometer (covering the wavelength range of $60\text{--}210 \mu\text{m}$) has been used to observe 1999 RQ₃₆.

The PACS photometer (Poglitsch et al. 2010) imaged the asteroid on September 9, 2011 (between 19:00 and 21:00 UT) at a heliocentric distance of 1.0146–1.0144 AU and a Herschel-centric distance of 0.1742 AU, and the phase angle was $85.3\text{--}85.4^\circ$. The time used for the observation was DDT-awarded specifically due to this optimum closest approach to Earth. The $70/160 \mu\text{m}$ scan-map observation was repeated ten times (5 times at scanangle 70° and 5 times at 110°), the $100/160 \mu\text{m}$ observation was repeated 14 times (7 times in each scanangle).

The PACS scan-map measurements were processed using HIPE 7.0 (Ott et al. 2009). The reduction steps were very similar to those used for trans-Neptunian objects (Santos-Sanz et al. 2012; Mommert et al. 2012; Vilenius et al. 2012), including corrections for moving targets. The final, single-repetition PACS maps (10 at $70 \mu\text{m}$, 14 at $100 \mu\text{m}$, and 24 at $160 \mu\text{m}$) have been median-averaged to remove (or at least decrease) the otherwise large instrumental noise. The background confusion noise has been eliminated as much as possible via techniques that have been developed for other moving sources (see detailed description in the electronic appendix in Santos-Sanz et al. 2012).

The derived fluxes were aperture- and colour-corrected to obtain monochromatic flux densities at the PACS reference wavelengths. The colour correction values for 1999 RQ₃₆ of 1.01, 1.02, 1.07 in blue ($70 \mu\text{m}$), green ($100 \mu\text{m}$) and red ($160 \mu\text{m}$) bands are based on a thermophysical model SED (spectral energy distribution), corresponding roughly to a 250 K black-body curve (PACS photometer passbands and colour correction factors, 2011). The flux calibration was verified by a set of five high-quality fiducial stars (β And, α Cet, α Tau, α Boo, and γ Dra), which were observed multiple times in the same PACS observing mode (PACS photometer - point source flux calibration, 2011).

The final values obtained for the PACS instrument datasets were deemed to be accurate within 5% based upon existing calibrations. The absolute flux calibration uncertainty is included in the values given in Table 1 (added quadratically to observational errors and errors related to aperture photometry). The fluxes given in Table 1 are colour-corrected, monochromatic flux densities at 70.0, 100.0, and $160.0 \mu\text{m}$, the three PACS reference wavelengths for the blue, green, and red bands, respectively. Figure 1 shows the combined PACS images aligned with the output from our thermal model of what PACS has observed during its observation campaign.

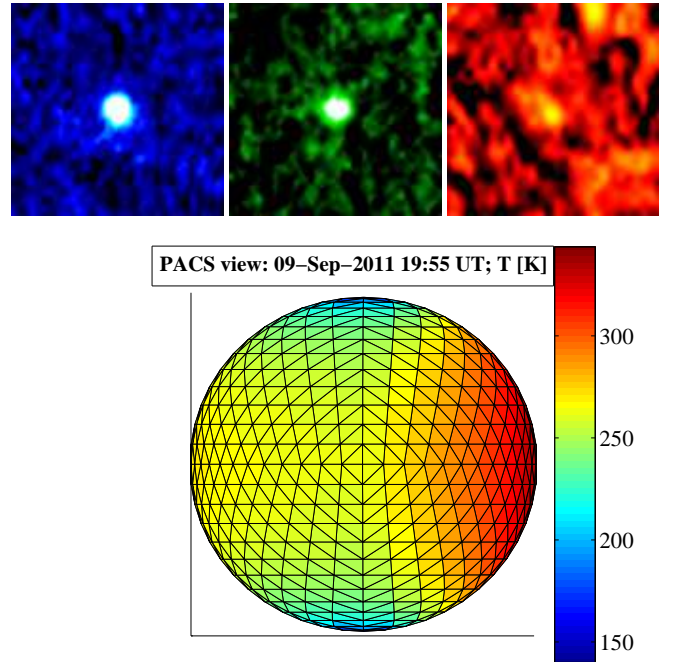


Fig. 1. The combined PACS images (top), at 70 (blue), 100 (green), and $160 \mu\text{m}$ (red), along with the output from our thermal model (bottom) of 1999 RQ₃₆, at the geometry of Herschel’s viewpoint. The shorter wavelengths effectively sampled the warmer facets of 1999 RQ₃₆’s surface, located in the subsolar region. Note that Herschel cannot spatially resolve the target.

2.2. ESO-VISIR observations and data processing

Besides the DDT awarded for Herschel, we also were awarded DDT to observe 1999 RQ₃₆ in September 2011 via ground-based N- and Q-band observations with the ESO-VISIR instru-

Table 1. Observation summary.

Start Time UT yyyy-mm-dd hh:mm:ss	Duration [sec]	Julian Date mid-time	λ_{ref} [μm]	FD [mJy]	FD _{err} [mJy]	r_{helio} r [AU]	Δ_{obs} [AU]	α [deg]	Observatory/ Instrument
2007-05-03 00:00:14	Start	2454223.50016				1.1237961	0.5056454	-63.5	Spitzer-PUI
...	11× 254	2454224.23335	16/22	Lightcurve		1.1262212	0.5089081	-63.3	Spitzer-PUI
2007-05-04 11:15:50	End	2454224.96655				1.1286398	0.5122203	-63.1	Spitzer-PUI
2007-05-03 21:39:13	4261	2454224.42689	5.2-38	SED		1.1268605	0.5097779	-63.2	Spitzer-IRS
2007-05-03 23:45:57	4260	2454224.51489	5.2-38	SED		1.1271494	0.5101723	-63.2	Spitzer-IRS
2011-09-09 19:01:12	1414	2455814.30068	70.0	27.0	1.7	1.0146021	0.1742221	+85.3	Herschel/PACS
2011-09-09 19:59:50	1414	2455814.34140	70.0	24.3	1.5	1.0144716	0.1742140	+85.4	Herschel/PACS
2011-09-09 19:25:49	1978	2455814.32104	100.0	14.2	1.1	1.0145368	0.1742180	+85.4	Herschel/PACS
2011-09-09 20:24:27	1978	2455814.36176	100.0	12.0	1.2	1.0144064	0.1742101	+85.4	Herschel/PACS
2011-09-09 19:25:49	1978	2455814.32104	160.0	6.5	2.3	1.0145368	0.1742180	+85.4	Herschel/PACS
2011-09-09 19:59:50	1414	2455814.34140	160.0	4.4	1.9	1.0144716	0.1742140	+85.4	Herschel/PACS
2011-09-09 20:24:27	1978	2455814.36176	160.0	7.6	2.0	1.0144064	0.1742101	+85.4	Herschel/PACS
2011-09-17 09:21:59	4× ~2 min	2455821.89306	8.59	23.7	3.6	0.9908803	0.1798955	+89.4	ESO VLT/VISIR

Notes. The eleven Spitzer-IRS Peak-up Images (PUI) have the AORKEYs 2141 2864/4400/4912/3120/5168/8240/3632/4144/4656/3888/3376. The data contain simultaneous 16 and 22 μm measurements. The re-reduced Spitzer-IRS data have the AORKEYs 21412352 and 21412608. They are separated by about half a rotation period. See also Emery et al. (2010) for more observational details and the presentation of preliminary results. The Herschel-PACS observations have the observation identifiers 1342228379 ... 1342228382, taken on Operational Day 849, the ESO VLT-VISIR observations are related to the programme-ID 287.C-5045(A).

ment (Lagage et al. 2004) mounted on the 8.2 m VLT telescope MELIPAL (UT 3) on Paranal.

The service-mode observers attempted twice to execute our four observing blocks in imaging mode, including each time the PAH1 (8.59 μm), NeII (12.81 μm), and the Q2 (18.72 μm) filters. The 1999 RQ₃₆ observations were done in parallel nod-chop mode with a throw of 8". Owing to poor observing conditions and difficulties during the target acquisition phase, combined with end-of-night constraints, the science observations were never executed. Nevertheless, we found 1999 RQ₃₆, with both the positive and two negative nod-chop beams on-chip, in the PAH1 target acquisition images taken on September 17, 2011 at an airmass of 1.79. We processed the four useful raw images using the ESO VISIR pipeline *Gasgano*¹ to produce a combined image suitable for aperture photometry. It was possible to calibrate those data using the standard star HD 217902 (9.923 Jy at 8.59 μm , taken at airmass 1.30) that was observed before the acquisition of 1999 RQ₃₆ and another one, HD 16815 (11.679 Jy at 8.59 μm , taken at airmass 1.40), which was observed the day after in the same filter and observing mode. Based on the derived count-to-Jy conversion factors and the experience from large calibration programmes (Schütz & Sterzik 2005), we were also able to correct for the airmass difference between the calibration stars and our science target. The counts decrease by about 10% for an airmass increase of 0.5. The fluxes of the standard stars and our target were extracted in an identical way to standard aperture photometry techniques. In the case of 1999 RQ₃₆ we checked that the first nod-chop pair was consistent with the second (i.e. that all three beams were in all the acquisition images) by also reducing them separately. The derived fluxes from each pair were consistent with those produced by combining both pairs together. We applied a colour correction of 1.004 (for 150-250 K blackbodies, considering the full atmosphere and bandpass transmission profiles) to the measured 1999 RQ₃₆ flux to obtain a mono-chromatic flux density at the PAH1 reference wavelength (see Table 1). For the error calculation (E. Pantin, M. van den Ancker & R. Siebenmorgen, priv. comm.), we quadrati-

cally added the following error sources: error in count-to-Jy conversion factor (2%), error of stellar model (2%), photometry error (10%), error of colour correction (2%), estimated additional uncertainty for measurements at airmass larger than 1.5 (5%), and flat-field error for an off-centre position in the acquisition images (10%), summing up to a total of 15% error in the derived flux density.

2.3. Observations of 1999 RQ36 with the Spitzer Space Telescope

To complete the dataset, we also analysed and utilised data from the Spitzer Space Telescope (Werner et al. 2004). Emery et al. (2010) present part of these observations, but the results were based on a preliminary data reduction alone.

Spitzer observed 1999 RQ₃₆ in different modes. Thermal IR spectra from 5.2 to 38 μm were taken with the Infrared Spectrograph (IRS) of opposite hemispheres of the body on 3/4 May 2007 21:42:03 - 22:46:57 (ID 21412352) and 23:48:51 - 00:53:40 UT (ID 21412608). Photometry at 16 and 22 μm was obtained with the IRS peak-up imaging (PUI) mode (IDs 21412864/4400/4912/3120/5168/8240/3632/4144/4656/3888/3376), taken at regular intervals between 3 May 2007 00:00:15 UT and 4 May 2007 11:11:37 UT. The 11 measurements cover the full rotation period uniformly. The phase angles, the heliocentric, and Spitzer-centric distances are given in Table 1.

The *Spitzer*-IRS observations were reduced with SPICE² in the recommended way following the data analysis cookbook for moving targets³. We used the PBCD-products⁴ from the Spitzer Heritage Archive SHA⁵, subtracted the background mea-

² <http://irsa.ipac.caltech.edu/data/SPITZER/docs/dataanalysis/> [May 7th, 2012]

³ <http://irsa.ipac.caltech.edu/data/SPITZER/docs/dataanalysis/> [May 7th, 2012]

⁴ Post-Basic Calibrated Data: Level 2 data

⁵ <http://sha.ipac.caltech.edu/applications/Spitzer/SHA/> [May 7th, 2012]

¹ <http://www.eso.org/gasgano>

measurements from the on-source measurements, and produced two spectra for each order in the short-low (SL) and long-low (LL) modules⁶, using the appropriate uncertainty and mask files. We averaged the resulting A-B and B-A spectra. The low flux in the SL2 range (5.2 to 7.5 μm) was averaged using a boxcar filter; in addition, we resampled the data in bins of uniform resolution $R = \lambda/\Delta\lambda$, with $R = 40$ (SL1: 7.6 to 14.3 μm) and $R = 30$ (SL2) to better measure the continuum signal of 1999 RQ₃₆ and to reduce the number of data points for the thermophysical model (TPM) analysis. For each bin we determined the weighted averaged wavelength, the median flux, and the root-sum-square of the propagated errors, including a 5% absolute flux calibration error as specified by the *Spitzer*/IRS team. Our derived fluxes and errors agreed within the given errorbars with the published figures in Emery et al. (2010) and are shown in Fig. 2.

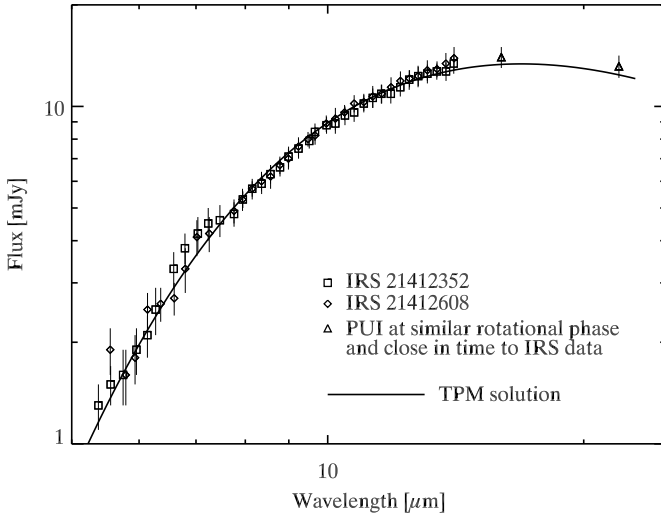


Fig. 2. Both *Spitzer* IRS spectra (SL-part only) are shown together with 2 PUI measurements taken close in time at similar rotational phases. Our best TPM solution is shown as a solid line.

2.4. Observation summary

In total, including the *Herschel*, *ESO-VISIR* and *Spitzer* dataset (see Table 1), we were able to place into our model a set of observations covering the wavelengths from 6 to 160 μm , phase angles of -63° , $+85^\circ$, and $+89^\circ$ (positive before opposition, negative after opposition), and covering nicely all rotational phases. For the TPM analysis (Sect. 3) we use the true observing and illumination geometries (*Spitzer*-, *Herschel*-, VLT-centric) for each measurement individually as given in Table 1. The importance of this dataset becomes clear in the coming section where it can be seen that our comprehensive coverage of wavelength and phase angle is key to extracting the main thermal parameters output from our thermal model.

⁶ Note, that we used only the SL-part of the observations. The LL part is more noisy and does not constrain our analysis in a significant way.

3. Thermophysical analysis of the observational data

We started the thermophysical model (TPM) analysis of the complete dataset by using a simple spherical shape model. For the object's rotation period we used 4.297812 ± 0.000001 hours (Nolan et al. 2012). Thermal data are very sensitive to the orientation of the spin axis (see e.g., Müller et al. 2011) and we used it as a free parameter in our analysis. Due to computing speed limitations we restricted this exercise to 60 different orientations for the rotation axis distributed over the entire sphere. The ecliptic latitude and longitude pairs to describe the spin vector orientation correspond to the 60 vertices of a mathematical description of a truncated icosahedron⁷ with 12 regular pentagonal faces and 20 regular hexagonal faces. To complete the picture, we added a few key spin axis orientations: pro- and retrograde rotations with the spin vector perpendicular to the ecliptic plane ($\beta_{\text{pole}} = \pm 90^\circ$), pole-on viewing geometries as seen during the *Spitzer*, the *Herschel*, and the *VISIR* observations, and another four orientations (with $\beta_{\text{pole}} < -70^\circ$) to explore the YORP spin-up equilibrium state (Vokrouhlický et al. 2003), which corresponds to the latest value derived by Nolan et al. (2012): The obliquity 180° case for the spin vector ($\beta_{\text{pole}} = -83.98^\circ$, $\lambda_{\text{pole}} = 92.17^\circ$) is very well covered by this set of different spin axis orientations, which included values of -78° , -80° , and -90° for β_{pole} (each time for a range of λ_{pole} values).

The spherical shape model with the almost 70 different spin axis orientations were imported into our TPM code (Lagerros 1996; 1997; 1998). Details about the techniques have recently been described in Müller et al. (2011) and O'Rourke et al. (2012). The TPM produces accurate thermal IR spectra and thermal lightcurves, taking a number of physical and thermal processes into account. In the TPM, the object is described by a given size, shape, spin-state, and albedo, placed at the true observing and illumination geometry. The TPM considers a 1-d heat conduction into the surface and allows surface roughness to be included, described by “f”, the fraction of the surface covered by spherical crater segments and “p”, the r.m.s. of the surface slopes, connected to the crater width-to-depth ratio (Lagerros 1998). A default setting (Müller et al. 1999) with $\rho=0.7$ and $f=0.6$ has been used as baseline.

The contributions of the subsurface emission at longer wavelength is accounted for by a wavelength-dependent emissivity decreasing from 0.9 at mid/far-IR (5 to 100 μm) to about 0.8 in the submillimetre/millimetre range of the spectrum, derived from a combined set of large main-belt asteroids (Müller and Lagerros 1998; 2002). Here, all radiometrically critical measurements are taken at wavelength below 100 μm , and there is no difference in using a constant emissivity of 0.9 or the wavelength-dependent emissivity model presented in Müller & Lagerros (2002).

For the full treatment of the energy balance on each surface facet within the model, we need to describe the amount of reflected light, described by the commonly used H-G-system (Bowell et al. 1989). The value for the absolute V-band magnitude H_V was determined by Krugly et al. (2002) and recently refined by Hergenrother et al. (2012). The best value of $H_V = 20.65$ mag was obtained by a linear phase function fit (phase slope $\beta = 0.039 \pm 0.005$ mag) to V-band photometry covering the phase angle range from 15° to 100° . Hergenrother et al. (2012) discuss the issue of a shallow opposition effect for low-albedo asteroids and conclude that a more realistic H_V -value for

⁷ http://en.wikipedia.org/wiki/Truncated_icosahedron

1999 RQ₃₆ would be 20.5 ± 0.3 mag. For G (slope parameter) we used the Krugly et al. (2002) value of 0.12.

Based on all available thermal data we searched for the best size and albedo solutions via well-established radiometric techniques (e.g., Harris & Lagerros 2002 and references therein) by using the above described settings. For each of the above spin vector orientations we calculated the reduced χ^2 -value for a wide range of typical thermal inertias (Delbo et al. 2007). We calculated the reduced χ^2 -values in the following way: $\chi^2_{\text{reduced}} = 1/(N-2) * \sum ((flx_{\text{obs}} - flx_{\text{mod}})/err_{\text{obs}})^2$, with N the number of degrees of freedom. Figure 3 shows the result of the analysis. The lowest χ^2 values are found for retrograde rotations ($\beta_{\text{pole}} < -70^\circ$) and thermal inertias around $600 \text{ J m}^{-2} \text{ s}^{-0.5} \text{ K}^{-1}$. The thermal inertia $3\text{-}\sigma$ confidence interval is from 400 to just above $1000 \text{ J m}^{-2} \text{ s}^{-0.5} \text{ K}^{-1}$. The $3\text{-}\sigma$ confidence interval $\chi^2 < (\chi^2_{\text{min}} + 3^2)$ is based on actual $\chi^2 = \sum ((obs - mod)/err)^2$ calculations (not the reduced χ^2 as shown in Fig. 3).

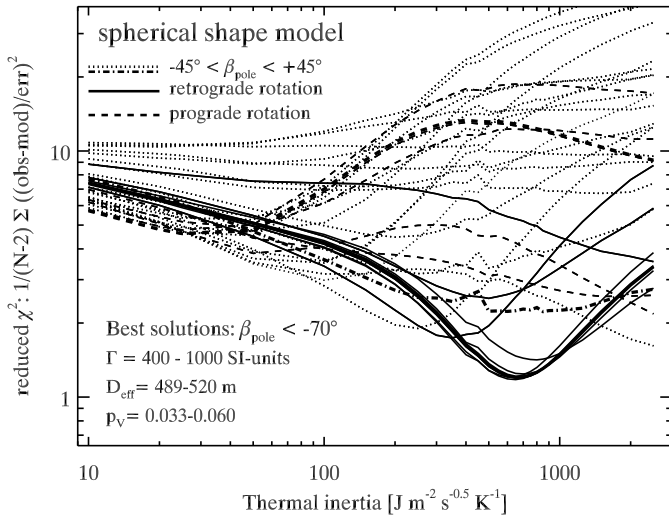


Fig. 3. χ^2 test for the full set of spin vector orientations and the full range of thermal inertias. The retrograde solutions with $\beta_{\text{pole}} < -45^\circ$ are given as solid lines, the prograde ones with $\beta_{\text{pole}} > +45^\circ$ as dashed lines, the ones where the latitude of the rotation pole is in the range $-45^\circ < \beta_{\text{pole}} < +45^\circ$ are shown in dotted lines. The thicker solid and dashed lines represent the $\beta_{\text{pole}} = \pm 90^\circ$ solutions, the thick dashed-dotted line the Herschel pole-on geometry.

Considering this possible Γ -range in combination with a spherical shape model and a pole axis pointing to the ecliptic south pole ($\beta_{\text{pole}} = -90^\circ$, retrograde rotation) leads to a size in the range 498 to 513 m and a geometric albedo p_v in the range 0.043 to 0.046. The true errors are larger: (i) the TPM fit to the observations is not perfect (mainly due to the spherical shape model), and the *r.m.s.* of all observation/model ratios (see Figs. 4 & 5) has to be included (dominating error contribution for the diameter); (ii) the solution also depends slightly on the selected spin vector orientation within the possible range $\beta_{\text{pole}} < -70^\circ$; (iii) the H-magnitude is given with an error of ± 0.3 mag (dominating error contribution for the albedo). Combining all errors quadratically led to an effective size of 503^{+17}_{-14} m for a spherical shape and a geometric albedo of $0.045^{+0.015}_{-0.012}$. These numbers are based on the assumption that 1999 RQ₃₆ has a “default roughness” that is typical of large main-belt asteroids (see also discussion in Section 4 below).

4. Discussions

4.1. Spin-axis orientation, sense of rotation

The before/after opposition data are the key element for extracting the sense of rotation. Our Herschel observations are all taken before opposition, i.e. leading the Sun (here positive phase angles). This means that Herschel has observed the target, while the unilluminated part of the surface was cold (see Fig. 1) corresponding to the pre-dawn part of the surface (for a retrograde sense of rotation). Spitzer has seen 1999 RQ₃₆ after opposition when the unilluminated part was still warm after it had rotated out of the Sun (see Fig. 7). The importance of the sense of rotation can clearly be seen in Fig. 3. The prograde rotation options produced very high values for the reduced χ^2 and can therefore be excluded with high confidence. The models with spin axes close to the ecliptic plane (including pole-on geometries) constrain the thermal inertia only very little; nevertheless, the reduced χ^2 -values are very high so these solutions can be ruled out. The TPM analysis clearly favours an axis orientation with $\beta_{\text{pole}} < -70^\circ$ in the ecliptic coordinate system. This agrees with the findings by Nolan et al. (2012) that the pole is close to the equilibrium state for the YORP effect (Vokrouhlický et al. 2003). 1999 RQ₃₆ has an orbit inclination of 6.02° , and Ω , the argument of ascending node, is 2.17° . The YORP predicted asymptotic zone with obliquity ϵ of 180° would therefore correspond to $\beta_{\text{pole}} = -83.98^\circ$ and $\lambda_{\text{pole}} = 92.17^\circ$ in our convention, very close to the south ecliptic pole.

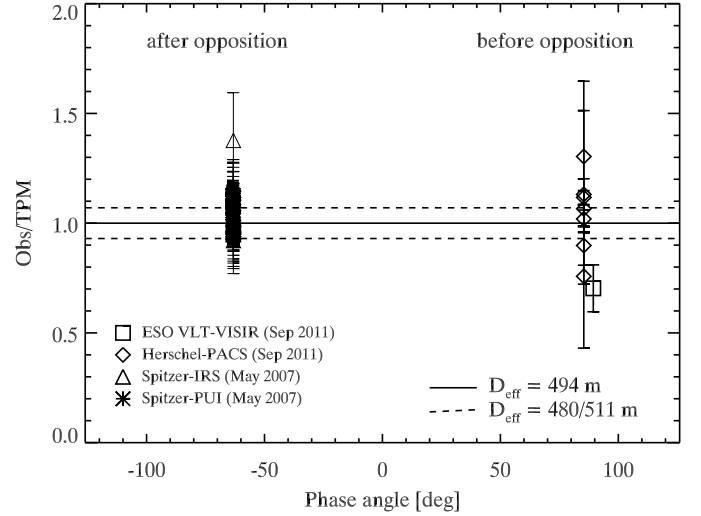


Fig. 4. Ratio between the observed fluxes and the corresponding TPM predictions as a function of phase angle (negative: after opposition; positive: before opposition). The model calculations are based on a thermal inertia of $600 \text{ J m}^{-2} \text{ s}^{-0.5} \text{ K}^{-1}$ and $\rho=0.2$ for the surface roughness. The VISIR data point can only be matched by assuming a higher surface roughness (see also Section 4.2 for further discussions).

4.2. Surface roughness

Due to the lack of observations close to opposition, our dataset does not constrain the surface roughness that plays a more dominant role at phase angles close to opposition very well (Müller 2002). In Section 3 we used the “default roughness” that was derived for large main-belt asteroids that are covered with a low

thermal conductivity regolith (Müller et al. 1999). To study the influence of roughness on the final size and albedo solutions, we analysed all thermal data, but this time for different levels of roughness. For simplicity, we assumed that 100% of the surface is covered by craters ($f=1.0$), which is a reasonable assumption considering that the model crater definition also includes micro-craters down to very small scales where the geometric optics approximation is still valid (Müller & Lagerros 1998). We varied the r.m.s. of the surface slopes ρ in steps of 0.1 from a perfectly smooth surface ($\rho=0.0$) to a very rough surface ($\rho=1.0$) and repeated our radiometric analysis. The reduced χ^2 -minima indeed reach acceptable values for almost all levels of roughness: A very low surface roughness with $\rho < 0.1$ would lead to a thermal inertia of $450 \text{ Jm}^{-2}\text{s}^{-0.5}\text{K}^{-1}$ which corresponds to an effective size of 490 m and a geometric albedo of $p_V = 0.047$. A surface roughness with $\rho > 0.9$ would point to a thermal inertia of $850 \text{ Jm}^{-2}\text{s}^{-0.5}\text{K}^{-1}$ with $D_{\text{eff}} = 508 \text{ m}$ and $p_V = 0.044$. This size range is entirely consistent with the possible range given by radar (Nolan et al. 2012), but it confirms that our dataset suffers from the degeneracy between surface roughness and thermal inertia. Figures 4 and 5 show the comparison between observations and model predictions assuming a roughness of $\rho=0.2$ (with $f=1.0$), similar to the moderate surface roughness (r.m.s. slopes $\sim 20^\circ$) used by Emery et al. (2010) to fit the IRS data.

The only data that do contain some information about roughness are the data at short wavelengths below $12 \mu\text{m}$ (IRS-spectrum and VISIR data point). The Wien part of the SED is strongly influenced by the hottest temperatures in the sub-solar region, while data at longer wavelengths beyond the thermal emission peak are more connected to the disk-averaged temperatures. This can be seen in Fig. 6: the low-roughness case fits the IRS-data very well (top of Fig. 6), but the model prediction for the VISIR data-point is overestimated by about 30%. If we use a high-roughness solution, then it is the other way round, where the VISIR data-point is well matched by the model prediction, but the IRS-spectrum divided by the corresponding model prediction shows a slight, wavelength-dependent mismatch (bottom of Fig. 6). The effects are small, and the VISIR data point has been taken in marginal conditions and as an acquisition frame. Also, modelling aspects like the implementation of surface roughness might play a role. The VISIR and IRS dataset are taken at very large and very different phase angles where the roughness effects on the IR beaming have not been studied very well. Nevertheless, the VISIR data point might indicate that we see variations in surface properties while the object is rotating. Based on the above specified rotation period, the two IRS spectra and the VISIR data are indeed taken at different rotational phases and correspond to different regions on the surface. A look at the reduced χ^2 -values seems to confirm this idea. The low-roughness model (top of Fig. 6) matches our thermal dataset very well (reduced χ^2 -values below 0.75), while the high roughness model (bottom of Fig. 6) clearly has problems with many of our data points (reduced χ^2 -values above 1.25), although it produces a perfect fit to the VISIR data point, which was taken at a unique rotational phase. But this aspect of surface roughness variations is clearly on vague grounds and should be confirmed via radar measurements or short-wavelength thermal lightcurves.

We should note here that the thermal emission at wavelengths shorter than $12 \mu\text{m}$ originates mainly in the hottest sub-solar region, which is equatorial in the case of 1999 RQ₃₆. Our speculation about possible surface roughness heterogeneity is therefore only related to a broad equatorial zone. Our dataset is not sensitive to roughness variations in the polar regions.

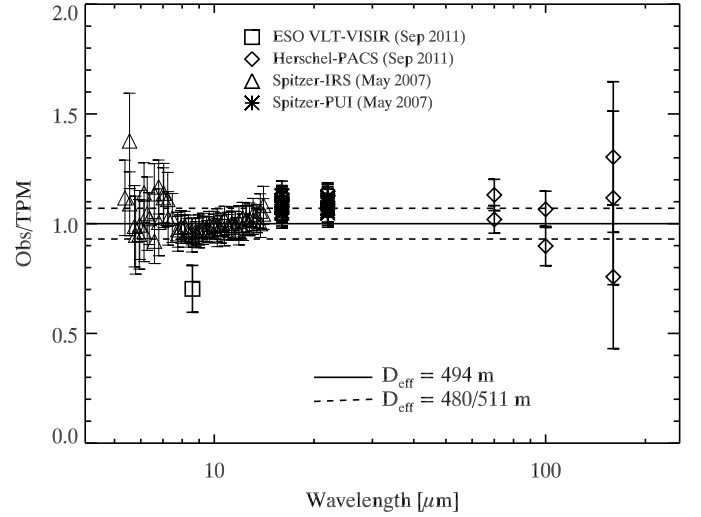


Fig. 5. Ratio between the observed fluxes and the corresponding TPM predictions as a function of wavelength.

Roughness can in principle be present on any scale. Radar observations from Goldstone and Arecibo in 1999 and 2005 revealed a featureless surface down to the radar resolution limit of 7.5 m (Hudson et al. 2000; Nolan et al. 2007), but so far the radar team(s) have not investigated whether there are also variations in surface roughness seen in the radar echoes (Mike Nolan, private communication).

4.3. Thermal inertia Γ

Pre- and post-opposition observations are the key to constraining the thermal inertia Γ , even more when the observations are taken at large phase angles (see Fig. 4). But, as described above, uncertainty remains because of the degeneracy between surface roughness effects and thermal inertia. From the exercise with different levels of roughness we find thermal inertias ranging from 450 to $850 \text{ Jm}^{-2}\text{s}^{-0.5}\text{K}^{-1}$. If we also include variations for the spin pole ($\beta_{\text{pole}} = -90^\circ \pm 20^\circ$), the possible confidence range lies between 350 to $950 \text{ Jm}^{-2}\text{s}^{-0.5}\text{K}^{-1}$, with the most likely value at $650 \text{ Jm}^{-2}\text{s}^{-0.5}\text{K}^{-1}$.

A closer inspection of possible thermal inertias confirms that thermal inertias outside this range cause a very obvious mismatch between the data taken before opposition (positive phase angles in our convention) and the ones taken after opposition (negative phase angles): A figure similar to Fig. 4, but with thermal inertias less than 350 or greater than $950 \text{ Jm}^{-2}\text{s}^{-0.5}\text{K}^{-1}$ would show a large imbalance between data taken before opposition and data taken after opposition. The determined Γ -range is close to the $600 \text{ Jm}^{-2}\text{s}^{-0.5}\text{K}^{-1}$ derived by Emery et al. (2010) for 1999 RQ₃₆ and also close to $\Gamma = 750 \text{ Jm}^{-2}\text{s}^{-0.5}\text{K}^{-1}$ derived for (25143) Itokawa (Müller et al. 2005). Such a thermal inertia value indicates regions with high conductivity, i.e. coherent boulders. It can therefore be expected that the surface of 1999 RQ₃₆ might show a similar texture to Itokawa's: with zones with different surface rock size distributions, though possibly with fewer large boulders that would have shown up as surface features in the radar measurements (Nolan et al. 2012). But, as discussed before, our results are only connected to the warm region where the measured thermal flux originates. Other parts of the surface -at very large and very low latitudes- could have very different thermal properties. Seismic vibrations or YORP-

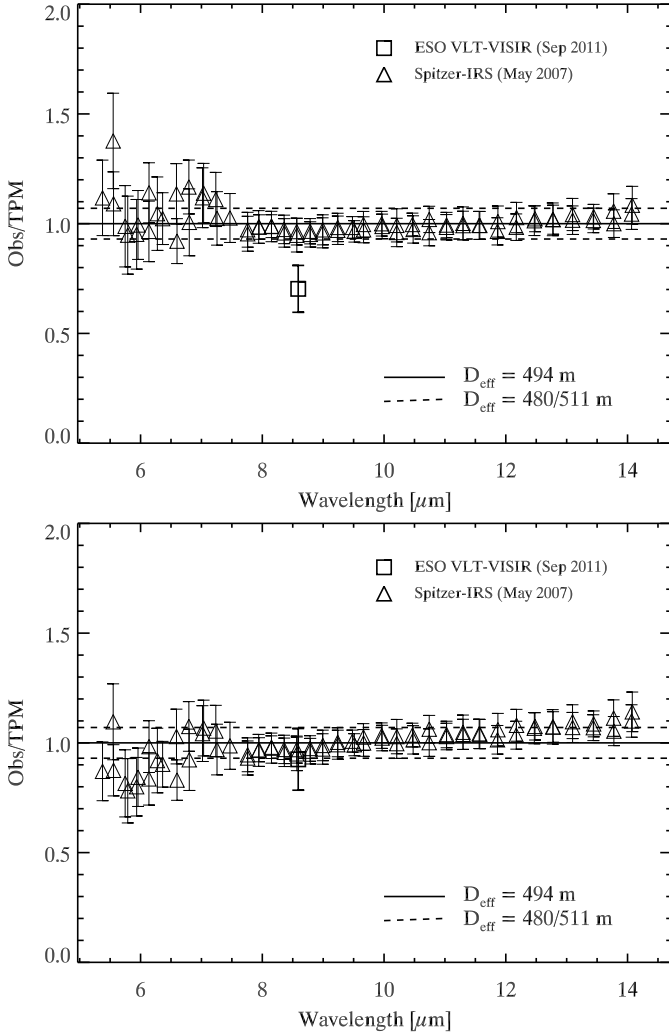


Fig. 6. Ratio between the observed fluxes and the corresponding TPM predictions as a function of wavelength. Top: assuming moderate surface roughness with a r.m.s.-slope of 0.2 gives a nice match to the 2 Spitzer-IRS spectra taken at opposite hemispheres (reduced $\chi^2 < 0.75$). Bottom: assuming a high surface roughness with a r.m.s.-slope > 0.8 gives a nice match to the VLT-VISIR data point, but there remains a slight trend with wavelengths for the IRS data which are taken at different rotation phases (reduced $\chi^2 > 1.25$).

introduced regolith turn-over (see Binzel et al. 2010, and references therein) could have influenced these “invisible” parts by moving material towards the equatorial region that we “see” in our thermal dataset. This means that our analysis does not preclude some regions with small grains.

4.4. Spheroidal or ellipsoidal shape

The visual lightcurves presented by Hergenrother et al. (2012) were taken at large phase angles between 60° and 70° and showed a low amplitude of 0.17 magnitudes and a trimodal shape. It is not possible to reproduce the observed lightcurve shape with a simple ellipsoidal shape model of uniform albedo, but small shape deviations in combination with high phase angles could explain the trimodal lightcurve. The lightcurve amplitude (at a phase angle of 65°) can be reproduced by a slightly deformed body with an axis ratio of $a/b=1.04$ and rotating around

a c-axis that points at the ecliptic south pole. We tested if such a rotating ellipsoid in combination with our derived mean thermal inertia of $600 \text{ Jm}^{-2}\text{s}^{-0.5}\text{K}^{-1}$ could also explain the two-band Spitzer-PUI thermal lightcurve (see also Figure 2 presented in Emery et al. 2010). Axis ratios a/b above about 1.1 (for the given spin vector and thermal inertia) can be excluded on basis of these 16 and $22 \mu\text{m}$ lightcurves.

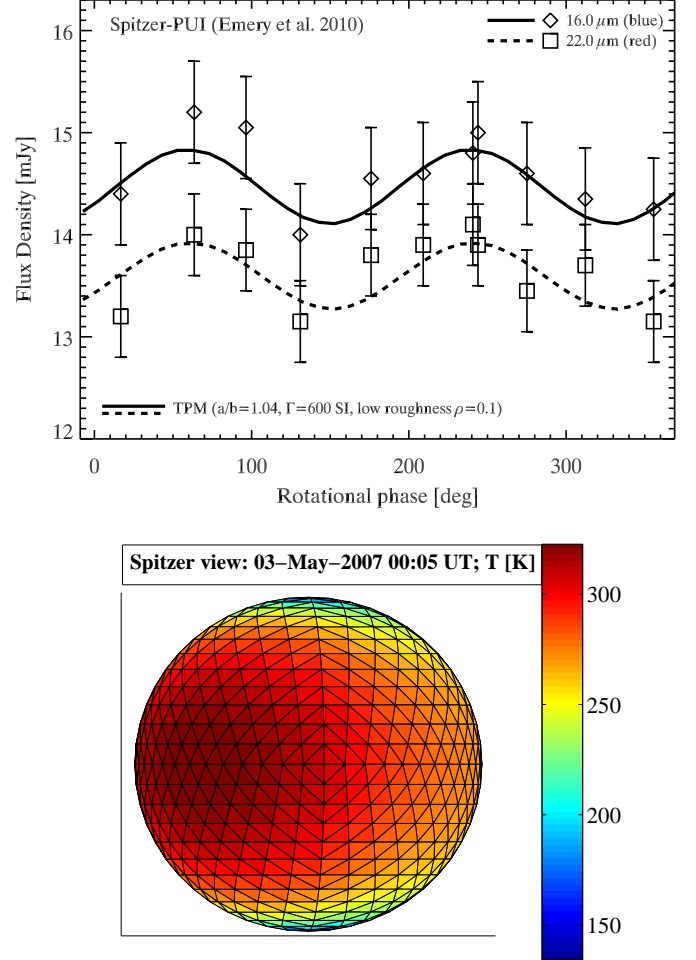


Fig. 7. Top: Spitzer-PUI data with the TPM prediction overplotted. Bottom: The corresponding output from our thermal model of 1999 RQ₃₆ as seen by Spitzer during its observation campaign. Spitzer cannot resolve the target spatially.

Figure 7 shows the result as a function of rotational phase. The zero rotational phase was determined in 10° steps via a χ^2 -test against the observational Spitzer-PUI data. The thermal lightcurve of a slightly elongated shape model with a 180° obliquity of the spin vector (combined with the derived low surface roughness and a thermal inertia of $600 \text{ Jm}^{-2}\text{s}^{-0.5}\text{K}^{-1}$) explains the different absolute flux levels at 16 and $22 \mu\text{m}$ very well and, at the same time, matches the two-band PUI thermal lightcurve and amplitude better than a simple spherical shape model. A lower thermal inertia would (for the given PUI observing geometry) increase the thermal lightcurve amplitude, a larger inertia would lower the amplitude. But the uncertainties of the individual PUI measurements and the remaining degeneracy with roughness do not allow constraining the thermal inertia even

more. Unfortunately, the application of our PUI-derived rotating ellipsoidal model directly to the PACS dataset was not successful. The PACS data cover about 1.5 h of the rotation period, but the quality of the PACS dataset with respect to S/N and time resolution is not sufficient to repeat the thermal lightcurve exercise as we did for the PUI data. The predicted 70.0 μm lightcurve amplitude is about 1 mJy peak-to-peak, while the flux error of the best 70.0 μm data point is already 1.5 mJy.

4.5. Size

The unknowns in surface roughness influenced the optimum thermal inertia slightly (see above), but the size and albedo values did not change significantly. We repeated the exercise shown in Fig. 3 with a low surface roughness (r.m.s.-slope $\rho = 0.2$), which produced the best match to the Spitzer-IRS data using a spherical and the ellipsoidal shape model specified above. The χ^2 values are now a few percent lower due to the better fit to the shortest wavelength data and, in the case of the ellipsoidal shape model, also a better match to the PUI data. The χ^2 -minimum is pointing towards a thermal inertia of $\Gamma = 650 \text{ Jm}^{-2}\text{s}^{-0.5}\text{K}^{-1}$, resulting in an equivalent diameter of an equal volume sphere of $D_{\text{eff}} = 494^{+11}_{-14} \text{ m}$ when we consider the full 3- σ confidence level for the thermal inertia. The VISIR data are better matched by a relatively high roughness. The derived corresponding values are then $D_{\text{eff}} = 508^{+3}_{-21} \text{ m}$ (at $\rho = 1.0$, $\Gamma_{\text{optimum}} = 850 \text{ Jm}^{-2}\text{s}^{-0.5}\text{K}^{-1}$). The equivalent size of 1999 RQ₃₆ (of an equal volume sphere) is therefore in the range between 480 to 511 m. The true size error is probably a bit larger because the equator-on observing geometry does not allow us to “see” the pole regions in the mid-to-far-IR thermal emission.

The derived diameter is significantly smaller than the 610 m derived from Spitzer measurements alone (Emery et al. 2010). Such a large size is clearly not compatible with the full set of thermal measurements. Emery (private communication) confirms that the published size was produced by a simple thermal model (NEATM, Harris 1998), which is known to overestimate the diameters of asteroids by 15-20% especially when the thermal dataset is limited to only large phase angles (Harris 2006).

It is interesting to note that Hudson et al. (2000) used the first Goldstone radar images -taken in 1999- to derive a diameter estimate of $\sim 500 \text{ m}$, very close to our value. Their preliminary results indicate a remarkably featureless surface (down to the resolution limit of 19 m) and an almost spherical object, but they derived a wrong spin period of $\sim 2 \text{ hr}$. Later on, Nolan et al. (2007) used multiple radar data from 1999 and 2005, some of them taken with unusually good aspect coverage, and conclude from the combined dataset that 1999 RQ₃₆ must be an irregular spheroid with about 580 m in diameter, more than 15% larger than our value. Only the recent work by Nolan et al. (2012) has brought the size back to the 500 m value.

4.6. Geometric albedo

The derived albedo is in the mid-range of values suggested for B-type asteroids (Tholen & Barucci 1989). But, as noted before, the albedo value depends directly on the H-magnitude. Our solution of $0.045^{+0.015}_{-0.012}$ already includes the error of ± 0.3 in H-magnitude. If it turns out that the opposition effect of 1999 RQ₃₆ is steeper or shallower than assumed for calculating of the H-magnitude, then the derived geometric albedo would also change. Hergenrother et al. (2012) provide, in addition to the above H-magnitude, H_V and G by strictly following the IAU

H-G photometric system for airless bodies (Bowell et al. 1989) and find $H_V = 19.90 \pm 0.10 \text{ mag}$ and $G = -0.14 \pm 0.02$. The corresponding radiometric size would not change, but the geometric albedo could then be as high as $p_V = 0.085$. The low albedos for near-Earth objects are believed to be connected to a primitive volatile-rich surface composition (Fernandez et al. 2005). But a dedicated orbital evolution and thermal history study by Delbo & Michel (2011) has shown that 1999 RQ₃₆ has approached the Sun in the past to regions of $q \leq 0.8$ (corresponding to about 400 K at the sub-solar point) with an 80% probability and with a lower probability even to $q \leq 0.6$ (480 K at the sub-solar point). Such high temperatures alter the pristine properties of the surface material, because some of the expected primitive compounds already break up at moderate temperatures above 300 K, and the surface volatiles might be completely lost (e.g., Marchi et al. 2009). But the temperature maxima at 3-5 cm below the surface are already lower by 100 K, and organics have very likely been protected from thermal break-up (Delbo & Michel 2011).

4.7. TPM concept

The calculations for the TPM beaming function for a rough surface are, strictly speaking, only applicable to the sunlit part of the asteroid (Lagerros 1998). A change in roughness changes the radiation field. A rougher surface has the tendency to emit or “beam” more in the solar direction at the expense of emission into larger phase angles. And this calculation is only done for the sunlit part of the surface. But even at large phase angles, the observed mid- and far-IR thermal emission is still dominated by the emission from the sunlit part of the object ($\sim T^4$), the emission from the dark and cold part beyond the terminator is negligible with or without roughness. Only for sub-millimetre/millimetre/centimetre wavelengths observations at very large phase angles above 90° are the night side contributions not negligible anymore, and these assumptions might turn out to be problematic and might result in wrong predictions. Müller et al. (2005) used observations up to 110° phase angle to derive highly accurate size and albedo values for 25143 Itokawa. The corresponding roughness and thermal inertia settings (similar to the values found here) explain the observations taken at 27° and 54° with a similar accuracy to the observations taken at 108 - 110° , giving us confidence that our TPM setup is appropriate also for the 1999 RQ₃₆ observations.

5. Conclusions

The Herschel DDT measurements of 1999 RQ₃₆, combined with ESO-VISIR DDT measurements and data from the Spitzer Space, have allowed us to conclude that this asteroid has a diameter of an equal volume sphere in the range 480 to 511 m, considerably smaller than previously estimated radar and radiometric values (Emery et al. 2010; Nolan et al. 2007), but in good agreement with the recent mean diameter given by Nolan et al. (2012) of $493 \pm 20 \text{ m}$. The thermal lightcurve variations are best-fit by an ellipsoidal shape model with a best fit a/b-ratio of 1.04, corresponding to an ellipsoidal body with $509 \times 489 \times 489 \text{ m}$ (\pm about 10 m in a - and b - and an unknown error in c -dimension). 1999 RQ₃₆ has a geometric albedo $p_V = 0.045^{+0.015}_{-0.012}$, in the nominal range for primitive volatile-rich NEAs of this type, and has a thermal inertia $\Gamma = 650 \pm 300 \text{ Jm}^{-2}\text{s}^{-0.5}\text{K}^{-1}$, similar to Itokawa, a rubble pile asteroid. Our results further serve to confirm that the asteroid has a retrograde rotation with a spin vector between -70 to -90° . The inconsistency between the flux value derived from VISIR observations and the Spitzer-IRS dataset, taken at

very different observing geometries, suggests there may be large variations in roughness on the surface. If the motion of surface material or regolith turnover processes are responsible for different terrains, then one can expect to find regions on the surface with very fresh material, at least at subsurface layers at several centimetres depth. The results of this work on the hypothesis that two different types of terrains exist with different levels of roughness and the possibility of having part of the surface with fine dust and pebbles is very important for the OSIRIS-REx mission sample mechanism strategy. A global mapping during the presampling phase will then allow the OSIRIS-REx team to select the most optimal area for collecting pristine and organic-rich material.

With this project we explore possibilities for thermophysical model techniques for an individual target that will soon be seen and characterised in detail. It will allow us to verify our findings on physical and thermal properties, as well as the proposed different surface terrains that are needed to explain the derived roughness and thermal inertia. Radiometric techniques are very powerful for deriving highly reliable size and albedo information, but signatures of surface texture, shape, spin-state, and thermal properties are also included in the object's thermal emission. In fact, because thermal data is (or will soon be) available for many thousands of asteroids (IRAS, MSX, ISO, Akari, Spitzer, WISE, ground-based mid-IR/submm/mm programmes, etc.), the results from 1999 RQ₃₆ can be considered to be the key to allowing us to transfer our model techniques to many other targets that will not be visited by spacecraft in the near future, but for which similar important questions can now be answered.

Acknowledgements. HSpot & HIPE are joint developments by the Herschel Science Ground Segment Consortium, consisting of ESA, the NASA Herschel Science Center, and the HIFI, PACS, and SPIRE consortia. We gratefully acknowledge the awarding of director discretionary time from the Herschel Space Observatory and ESO to support the work published here. We would also like to acknowledge the generous support by Mario van den Ancker (ESO) for installing and running of the VISIR pipeline and the support by Eric Pantin (CEA) and Ralf Siebenmorgen (ESO) for VISIR calibration and error calculation issues. Support for the Spitzer data reduction was provided by Sonia Fornasier, Josh Emery, and Jeffrey Van Cleve. It is also our pleasure to thank the Herschel Science Centre Mission Planning Team for their efforts in the optimal scheduling of these observations. Cs. K. and A. P. are supported by the ESA Grant PECS-98073 and by the Bolyai Research Fellowship of the Hungarian Academy of Sciences. We would also like to thank the anonymous referee for a very thorough and very constructive review of the manuscript.

References

- Binzel, R.P., Morbidelli, A., Merouane, S. et al. 2010, *Nature*, 463, 331
- Bowell, E. 1989, *Asteroids II*; Proceedings of the Conference, Tucson, AZ, Mar. 8-11, 1988 (A90-27001 10-91), University of Arizona Press, 1989, p. 524-556
- Campins, H., Morbidelli, A., Tsiganis, K. et al. 2010, *ApJ*, 721, 53
- Cellino, A., Zappalà, V., Doressoundiram, A. et al. 2001, *Icarus*, 152, 225-237
- Clark, B. E., Binzel, R. P., Howell, E., et al. 2011, *Icarus*, 216, 462-475
- Delbó, M., Dell'Oro, A., Harris, A. W. et al. 2007, *Icarus*, 190, 236
- Dombard, A. J., Barnouin, O. S., Prockter, L. M. & Thomas, P. C. 2010, *Icarus*, 210, 713
- Emery, J. P., Fernández, Y. R., Kelley, M. S., et al. 2010, 41st LPSC, LPI contribution No. 1533, 2282
- Fernández, Y. R., Jewitt, D. C., Sheppard, S. S. 2005, *AJ*, 130, 308
- Harris, A. W. 1998, *Icarus* 131, 291
- Harris, A. W. & Lagerros, J. S. V. 2002, *Asteroids III*, W. F. Bottke Jr., A. Cellino, P. Paolicchi, and R. P. Binzel (eds), University of Arizona Press, Tucson, p.205-218
- Harris, A. W. 2006, in *Asteroids, Comets, Meteors*, eds. D. Lazzaro, S. Ferraz-Mello & J. A. Fernández, Proc. IAU Symp., 229, 2005
- Hergenrother, C. W., Nolan, M., d'Aubigny, C. et al. 2012, LPS XXXXIII, Abstract #2219
- Hudson, R. S., Ostro, S. J., Benner, L. A. M. et al. 2000, AAS DPS # 32, #07.10, BAAS 32, 1001
- Krugly, Y. N., Belskaya, I. N., Shevchenko, V. G. et al. 2002, *Icarus*, 158, 293-304
- Lagage, P. O., Pel, J. W., Authier, M. et al. 2004, *The Messenger* 117, 12-16
- Lagerros, J.S.V., 1996, *A&A*, 310, 1011-1020
- Lagerros, J.S.V., 1997, *A&A*, 325, 1226-1236
- Lagerros, J.S.V., 1998, *A&A*, 332, 1123-1132
- Lauretta, D. S., Drake, M. J., Binzel, R. P., et al. 2010, *M&PSA*, 73, 5153
- Lauretta, D. S. & The OSIRIS-REx Team 2012, LPS XXXXIII, Abstract #2491
- Marchi, S., Delbó, M., Morbidelli, A. et al. 2009, *MNRAS* 400, 147-153
- Delbo, M. & Michel, P. 2011, *ApJL*, 728, 42
- Milani, A., Chesley, S. R., Sansaturio, M. E. et al. 2009, *Icarus* 203, 460
- Mommert, M., Harris, A. W., Kiss, C. et al. 2012, *A&A*, accepted
- Müller, T. G. & Lagerros, J. S. V. 1998, *A&A*, 338, 340-352
- Müller, T. G., Lagerros, J. S. V., Burgdorf, M. et al. 1999, in *The Universe as Seen by ISO*. Eds. P. Cox & M. F. Kessler, ESA-SP 427, 141-144
- Müller, T. G. & Lagerros, J. S. V. 2002, *A&A*, 381, 324-339
- Müller, T. G. 2002, *M&PS*, 37, 1919
- Müller, T. G., Sekiguchi, T., Kaasalainen, M. et al. 2005, *A&A*, 443, 347-355
- Müller, T. G., Durech, J., Hasegawa, S. et al., 2011, *A&A*, 525, A145
- Nolan, M. C., Magri, C., Ostro, S. J. et al. 2007, AAS DPS # 39, #13.06, BAAS 39, 433
- Nolan, M. C., Magri, C., Benner, L. A. M. et al. 2012, ACM 2012 abstract # 6345, <http://www.lpi.usra.edu/meetings/acm2012/pdf/6345.pdf>
- O'Rourke, L., Müller, T. G., Valtchanov, I. et al. 2012, *P&SS*, accepted
- Ostro, S. J., Margot, J.-L., Benner, L. A. M. et al. 2006, *Science*, 314, 1276-1280
- Ott, S. 2009, *Herschel Interactive Processing Environment, HIPE*, Proceedings of the Astronomical Data Analysis Software and Systems XIX Conference, 434, 139-142
- PACS photometerPoint Source Flux Calibration, Müller et al. 2011, PICC-ME-TN-037, Version 1.0, retrieved 29/Feb/2012; technical report available via URL:http://herschel.esac.esa.int/twiki/bin/view/Public/PacsCalibrationWeb/pacs_bol
- PACS Photometer Passbands and Colour Correction Factors for Various Source SEDs, Müller, T., Okumura, K., Klaas, U. 2011, PICC-ME-TN-038, Version 1.0, retrieved 29/Feb/2012; technical report available via URL:http://herschel.esac.esa.int/twiki/pub/Public/PacsCalibrationWeb/cc_report_v1.p
- Pilbratt, G. L., Riedinger, J. R., Passvogel, T. et al. 2010, *A&A*, 518, L1
- Poglitsch, A., Waelkens, C., Geis, N. et al. 2010, *A&A*, 518, L2
- Santos-Sanz, P., Lellouch, E., Fornasier, S. et al. 2012, *A&A*, accepted
- Schütz, O. & Sterzik, M. 2005, in *High Resolution Infrared Spectroscopy in Astronomy*, Proceedings of an ESO Workshop held at Garching, Germany, 18-21 November 2003. Käufel, Siebenmorgen, Moorwood (Eds.), 104
- Tholen, D. J. & Barucci, A. M. 1989, *Asteroids II*; Proceedings of the Conference, Tucson, AZ, Mar. 8-11, 1988 (A90-27001 10-91), University of Arizona Press, 1989, p. 298-315
- Vilenius, E., Kiss, C., Mommert, M. et al. 2012, *A&A*, submitted
- Vokrouhlický, D., Nesvorný, D., Bottke, W. F. 2003, *Nature*, 425, 147
- Walsh, K. J., Richardson, D. C. & Michel, P. 2008, *Nature* 454, 188-191
- Werner, M. W., Roellig, T. L., Low, F. J. et al. 2004, *ApJS*, 154, 1